

# StoX-Net: Stochastic Processing of Partial Sums for Efficient In-Memory Computing DNN Accelerators

Ethan G Rogers\*  
Sohan Salahuddin Mugdho\*  
Kshemal Kshemendra Gupte  
Cheng Wang  
Iowa State University of Science and Technology  
Ames, Iowa, USA

## ABSTRACT

Crossbar-based in-memory computing (IMC) has emerged as a promising platform for hardware acceleration of deep neural networks (DNNs). However, the energy and latency of IMC systems are dominated by the large overhead of the peripheral analog-to-digital converters (ADCs). To address such ADC bottleneck, here we propose to implement stochastic processing of array-level partial sums (PS) for efficient IMC. Leveraging the probabilistic switching of spin-orbit torque magnetic tunnel junctions, the proposed PS processing eliminates the costly ADC, achieving significant improvement in energy and area efficiency. To mitigate accuracy loss, we develop PS-quantization-aware training that enables backward propagation across stochastic PS. Furthermore, a novel scheme with an inhomogeneous sampling length of the stochastic conversion is proposed. When running ResNet20 on the CIFAR-10 dataset, our architecture-to-algorithm co-design demonstrates up to 22x, 30x, and 142x improvement in energy, latency, and area, respectively, compared to IMC with standard ADC. Our optimized design configuration using stochastic PS achieved 666x (111x) improvement in Energy-Delay-Product compared to IMC with full precision ADC (sparse low-bit ADC), while maintaining near-software accuracy at various benchmark classification tasks.

## KEYWORDS

In-Memory Computing, Deep Neural Networks, Hardware Accelerators, Stochastic Computing

## ACM Reference Format:

Ethan G Rogers, Sohan Salahuddin Mugdho, Kshemal Kshemendra Gupte, and Cheng Wang. 2024. StoX-Net: Stochastic Processing of Partial Sums for Efficient In-Memory Computing DNN Accelerators. In *Proceedings of ACM / IEEE Journal/Conference (In Preparation'24)*. ACM, New York, NY, USA, 7 pages. <https://doi.org/10.1145/nnnnnnn.nnnnnnn>

\*Both authors contributed equally to this work.

Permission to make digital or hard copies of all or part of this work for personal or classroom use is granted without fee provided that copies are not made or distributed for profit or commercial advantage and that copies bear this notice and the full citation on the first page. Copyrights for components of this work owned by others than the author(s) must be honored. Abstracting with credit is permitted. To copy otherwise, or republish, to post on servers or to redistribute to lists, requires prior specific permission and/or a fee. Request permissions from [permissions@acm.org](mailto:permissions@acm.org).

*In Preparation'24, July 2024, Washington, DC, USA*

© 2024 Copyright held by the owner/author(s). Publication rights licensed to ACM.

ACM ISBN 978-x-xxxx-xxxx-x/YY/MM

<https://doi.org/10.1145/nnnnnnn.nnnnnnn>

## 1 INTRODUCTION

Crossbar-based analog in-memory computing (IMC) has demonstrated great potential for Deep Neural Network (DNN) acceleration by achieving high efficiency and massive parallelism at processing matrix-vector-multiplications (MVMs)[19], which dominates most state-of-the-art DNN workloads[4]. However, the hardware cost of large-scale IMC systems is dominated by the significant overhead of peripheral analog-to-digital converters (ADCs), which is required to ensure robust data communication in a large-scale system. ADC consumes over 60-80% of the energy and chip area of IMC hardware [3, 19]. Due to the large area overhead of high-precision A-D conversion, an ADC must be shared by multiple columns in a crossbar. Such design leads to a severe throughput bottleneck since the processing of the array-level outputs across multiple columns has to be done sequentially.

While various recent works have aimed to mitigate the ADC bottleneck [6, 17, 26], minimizing ADC overhead in IMC while still maintaining satisfactory inference accuracy remains a significant challenge. Various factors contribute to the difficulty in addressing the ADC bottleneck. (1) First, since the array-level partial sums (PS) are not represented at the application level, the standard quantization approach focusing on activation and weights can not directly address the ADC precision for PS. (2) Second, while quantization-aware training is effective at enabling hardware-friendly models, training with PS quantization desires backward propagation with careful incorporation of array-level variables, which requires re-designing the computational graph of the DNN model. (3) Third, the required ADC bit precision for MVM may vary significantly depending on both the algorithmic attributes (such as sparsity and DNN layer dimension) and hardware attributes (such as array size and bits per memory cell). Accommodating these varying scenarios requires reconfigurability and flexibility in ADC, leading to increased overhead and design complexity.

In this work, we propose **stochastic processing** of the array-level partial sum for efficient IMC leveraging a spin-orbit-torque magnetic tunnel junction (SOT-MTJ) with simple circuitry such as an inverter. To address the accuracy drop due to loss of information at the stochastic PS, a PS-aware training methodology with the stochastic switching behavior of SOT-MTJs is developed. The low-overhead crossbar peripheral based on the proposed spintronic devices/circuits demonstrates significant improvement in energy efficiency and considerable area savings. Our proposed IMC design eliminates the ADC bottleneck and opens up an exciting direction

where stochastic computation could play a vital role in designing ultra-efficient non-von Neumann ML accelerators. The major contributions of our work are the following:

- We propose StoX-Net, an IMC architecture with aggressively quantized array-level partial sums based on stochastic switching dynamics of SOT-MTJs with simple CMOS peripherals. The ADC bottleneck in IMC is eliminated, leading to significant improvement in hardware efficiency.
- We develop a comprehensive framework of PS quantization-aware training that addresses the accuracy degradation due to the stochastic conversion. In particular, both the device-level stochastic MTJ switching behavior, and key architectural attributes including bit slicing and array size, are incorporated into backward propagation. Our model with 1-bit stochastic PS achieves (or slightly exceeds) state-of-the-art accuracy at benchmarking image classification tasks.
- We identify that the state-of-the-art quantization of convolutional DNN has severe limitations due to the **first convolution layer remaining at high precision**. The first convolution layer is typically compute-intensive and dominates the total computation of DNN. To address this challenge, we explore layer-wise inhomogeneous sampling numbers to enable aggressive PS quantization on the first convolution layer. Our inhomogeneous stochastic sampling based on a Monte-Carlo-based sensitivity analysis achieves improvement in accuracy with minimal additional overhead, demonstrating an advantageous trade-off.

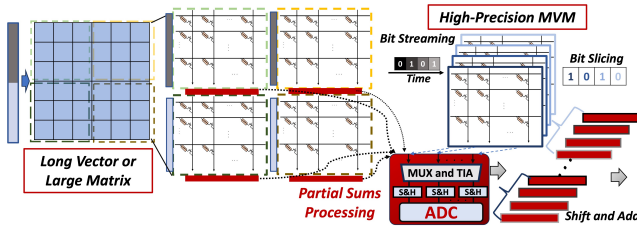


**Figure 1:** ADC bottleneck incurred at the partial sum processing in IMC crossbar architecture.

## 2 BACKGROUND

### 2.1 DNN acceleration with in-memory computing

Analog IMC is being extensively explored for accelerating DNN inference to meet the growing computational demand. With the weight matrices stored in crossbar arrays, the data movement of MVM processing is drastically reduced, alleviating the von Neumann memory bottleneck. To process a large-scale DNN workload, large matrices and high-precision MVMs need to be partitioned into multiple crossbar arrays. To ensure robust data communication, an analog crossbar IMC macro is connected with other components through digital-to-analog-converters (DAC) at the input and ADC at the crossbar output. The resolution of DAC at each row is typically designed at 1 bit for area saving, while high-precision input activation will be converted to bit streams over multiple time steps (bit streaming). As for high-precision weights, due to the technological limitation in the number of bits per cell, a full-precision

weight matrix will be partitioned into several slices of sub-arrays (bit slicing).

The required ADC solution  $N$  for array-level PS processing is  $N = \log_2(N_{row}) + I + W - 2$ , where  $N_{row}$  is the number of activated rows;  $I$  is input bits per stream; and  $W$  is bits per slice. Since the energy, area, and latency overhead of ADC increase significantly with bit precision [14], ADC becomes the bottleneck of efficiency and performance in IMC design.

### 2.2 Stochastic spintronics for machine learning

Several emerging NVM technologies, including resistive memory (ReRAM) and magnetic random access memory (MRAM), have been explored for machine learning acceleration. Recent explorations have demonstrated that spintronic devices exhibit sufficient endurance to realize both synaptic weight storage and neural activation. [7] Particularly, an SOT-MTJ under an excitation current with varying magnitude will have the magnetization switching probability as a sigmoidal function of the current, which provides a direct emulation of a stochastic neuron [18] with significantly higher area/energy efficiency compared to CMOS implementations. Moreover, the separate read/write paths of SOT-MTJs offer immense design flexibility by eliminating the constraint of write current density[20]. All-spin neuro-synaptic processors based on stochastic switching of SOT-MTJ have been proposed [21]. We will explore SOT-MTJs for efficient PS processing of the crossbar output.

### 2.3 Related work on addressing the ADC bottleneck in IMC

Various works have investigated co-designing the IMC hardware architecture and DNN algorithms to reduce the ADC precision. One major thrust focuses on exploiting quantization with hardware-aware training. In [10, 12] binary neural networks exhibit improved efficiency for IMC, but the models are limited to 1-bit representation. Recent works [9, 11, 17] implemented bit slicing/streaming to map workloads with multi-bit weights/activations. Aggressively reducing the ADC precision to 1-bit will essentially enable using sense amplifiers. However, 1-bit PS showed sizeable accuracy degradation even after hardware-aware re-training [9, 11]. Moreover, it is important to note that the state-of-the-art quantization-aware training models keep the first convolution layer **at full precision** [13, 16, 17]. However, the compute-intensive first convolution layer in image processing can dominate the overall computation workloads. Keeping a full-precision first layer severely limits the overall improvement in energy and throughput.

Another major thrust is to exploit sparsity through pruning and re-training to enable lower ADC precision [8, 26]. Higher sparsity reduces the range of possible values of MVM output and thus reduces the ADC resolution requirement. As a result, sparsity-aware IMC with reconfigurable ADC resolution can improve energy and latency. However, it is important to note that the *area* of the peripheral ADC circuitry remains large in order to handle the *highest* bit precision of the reconfigurable design. Such large area overhead still hinders the hardware parallelism in IMC architecture.

Compared to related works, our proposed StoX-Net exhibits distinctive characteristics. First, we, for the first time, represent the array-level PS by hardware-inspired stochastic bits, and incorporate the stochastic representation into training with bit slicing.

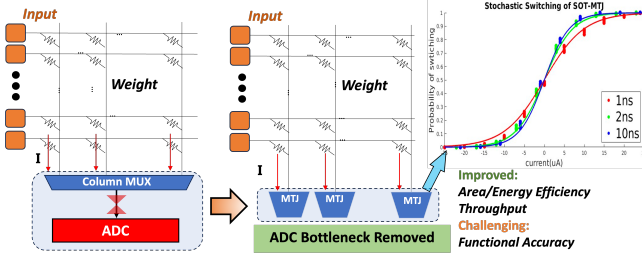


**Figure 2:** The overview of the proposed crossbar MVM processing with stochastic MTJ.

Second, we leverage the sampling of stochastic bits to provide re-configurability in the conversion precision without sacrificing the area efficiency and hardware parallelism. Third, to achieve better scalability to larger-scale input, we venture into aggressive PS quantization of the first convolution layer and demonstrate a balanced performance of accuracy and hardware efficiency.

### 3 IMC WITH STOCHASTIC PARTIAL SUMS

The proposed StoX-Net is built on IMC crossbar arrays where current-voltage converters, column-shared MUXs, and peripheral ADCs are replaced by a row of stochastic SOT-MTJs (Fig. 2). We first present the device/circuit design of our stochastic PS processing components and then implement stochasticity-aware training of quantized DNNs with bit slicing considered [13, 16].

#### 3.1 Stochastic PS processing based on MTJ

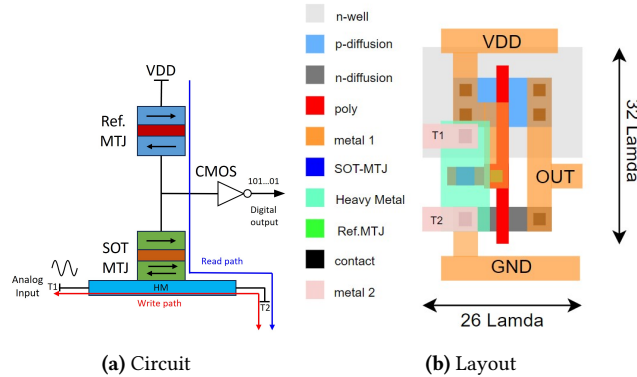


**Figure 3:** Stochastic MTJ-converter

The stochastic processing based on the current-driven probabilistic switching of SOT-MTJs is shown in Fig. 2. The device behavior is simulated using a MATLAB-based macro-spin Landau Lifshitz Gilbert (LLG) equation simulator with the SOT current included. Using an MTJ with tunnel magnetoresistance ratio (TMR) of 350-450% [20], a simple voltage divider circuit combined with a CMOS inverter can behave as a stochastic binary analog to digital converter as shown in Fig. 3a.

The area of the stochastic MTJ converter is obtained based on the layout in Fig. 3b. The layout is drawn following the  $\lambda$ -based design rules [1], where  $\lambda$  is half the feature size. Considering a 28 nm feature size, the area can be estimated as  $A = 32\lambda * 26\lambda = 0.0163 \mu\text{m}^2$ .

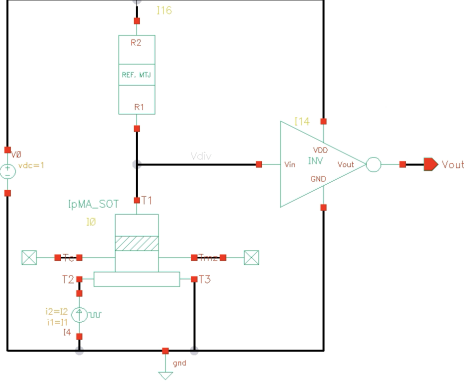
Parameter	Value
SOT-MTJ dimension	90nm x 70nm x 2.5nm
$R_{LRS}$	180 k $\Omega$
TMR	4.4
$t_{ox}$	1.46 nm
HM resistivity ( $\rho$ )	160 $\mu\Omega\text{cm}$ [20]
HM dimensions	144nm x 112nm x 3.5nm
$I_{write}$	0 - $\pm 100\mu\text{A}$
VDD	1 V
Ref. MTJ resistance	435 k $\Omega$

**Table 1:** Device parameters

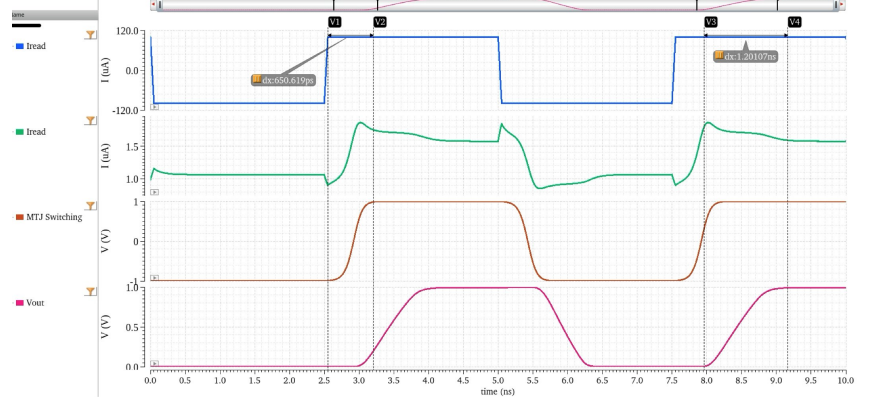
The capability of the stochastic MTJ-converter is illustrated in Fig. 4. For simulating the SOT-MTJ, we use a modified version of the STT-SOT-MTJ model developed by the Spintronics Interdisciplinary Center (Spinlib) [23]. The MTJ-converter features a 435k $\Omega$  reference MTJ and a free SOT-MTJ device arranged as a voltage divider. The SOT-MTJ receives pulses of 100 $\mu\text{A}$  and -100 $\mu\text{A}$  of 2.5ns each to imitate the crossbar current. The SOT-MTJ switches its state when 100 $\mu\text{A}$  is supplied and resets with an equivalent negative current. This current modulation alters the SOT-MTJ's resistance state, affecting the voltage division ratio with the reference resistor. The midpoint voltage of this divider varies due to the SOT-MTJ's state and is used as the input to an inverter, and the corresponding output has distinct '0' and '1' voltage levels. The sizing of the transistors in the inverter is optimized by minimizing the width to ensure distinct and clear output levels corresponding to the voltage variations from the divider. The MTJ's resistance is adjusted by varying its dimensions and the thickness of the oxide layer  $t_{ox}$  to achieve a parallel low state resistance  $R_{LRS}$  of 180k $\Omega$  and an anti-parallel high state resistance  $R_{HRS}$  of 970.2k $\Omega$ , with a TMR of 4.4. The SOT-MTJ's elliptical shape enhances the efficiency and reliability of the switching process by optimizing the magnetic field distribution within the junction. Our simulations reported a write latency of 650.6ps and read latency of 1.2ns, indicating rapid response times suitable for high-frequency applications. Energy consumption was measured at 5.695fJ per conversion cycle by calculating the total power consumption for one period. The device operates over a temperature range of -30 $^{\circ}\text{C}$  to 300 $^{\circ}\text{C}$ , emphasizing the robustness and potential versatility of the MTJ device in various environmental conditions. As Demonstrated in the following sections, the proposed SOT-MTJ-based converter is orders of magnitude more energy and area-efficient than ADC, leading to significant improvement of system-level hardware efficiency compared to standard IMC.

#### 3.2 Hardware-Aware Training of Quantized DNN with Stochastic Partial Sum

We map large DNN workloads into crossbars with finite array size and limited bits per cell with bit slicing from [19] and input/weight representation from [17]. Mapping a convolution layer of kernel size  $K_h * K_w$  and  $C_{in}$  input channels using a crossbar array of  $R_{arr}$  rows results in a number of subarrays defined by  $N_{arrs} = \text{ceil}(\frac{K_h * K_w * C_{in}}{R_{arr}})$ . For bit slicing, we consider 1-, 2-, and 4-bit per memory cell in the StoX-Net design. Based on Algorithm 1, a software-level MVM operation with the number of weight and



(a) Schematic



(b) Waveforms

**Figure 4:** Schematic implementation of the stochastic MTJ-converter. (4a) shows the circuit schematic of the converter. The SOT-MTJ model developed by Spinlib [23] has been used in the circuit. (4b) shows the input and output waveforms of the converter.

input slices being  $W_s$  and  $A_s$ , will have  $A_s * W_s$  array-level PSs to be shift-and-added ( $S&A$ ). In addition to workload partitioning, StoX-Net also considers SOT-MTJ samplings in its optimization.

**Algorithm 1** Crossbar MVM with Stochastic Partial Sum

**Input:**

$A_l \in [-1, 1], A_b, A_s \in [1, A_b], W_l \in \mathfrak{R}, W_b, W_s \in [1, W_b], R_{arr} = \max$  subarray column length

**Output:** hardware-aware  $O_l$

```

 $N_{arrs} \leftarrow \text{ceil}(\frac{K_h * K_w * C_{in}}{R_{arr}})$       ▷ Determine # of PS subarrays
 $W_{dims} \leftarrow (C_{out} * W_s, C_{in}, K_h, K_w)$ 
 $A_q \leftarrow Q(A_l, A_b)$                         ▷ Quantize  $W_l, A_l$ 
 $W_q \leftarrow Q(\text{bn}(W_l), W_b)$                 ▷  $\text{bn}(W_l)$  column-wise
 $A_q^N \leftarrow \text{Split}(A_q, N_{arrs}, A_s)$         ▷ Partition to subarrays
 $W_q^N \leftarrow \text{Split}(W_q, N_{arrs}, Q_s)$ 
for  $i \in [0, N_{arrs})$  do
  for  $j \in [0, N_{samples})$  do                ▷ multisampling
     $O_{i,j} \leftarrow \text{MTJ}(\text{MVM}(W_q^i, A_q^i))$     ▷ Perform Conv MVMs
     $O_{i,j}^{S\&A} \leftarrow S\&A(\frac{O_{i,j}}{N_{arrs} * N_{samples}})$   ▷ Reduce to  $C_{out}$ 
     $O_l \leftarrow O_l + O_{i,j}^{S\&A}$ 
  end for
end for

```

To process the crossbar output using the SOT-MTJ, the curve of switching probability versus current is emulated by the  $\tanh$  function:

$$\text{MTJ}(x) = \begin{cases} 0 & \tanh(\alpha x) < \text{rand} \\ 1 & \tanh(\alpha x) \geq \text{rand} \end{cases} \quad (1)$$

where  $\alpha$  is the sensitivity parameter. Increasing  $\alpha$  will make the tanh curve more step-like, approaching a deterministic sense amplifier. The effective sensitivity can be altered by tuning the range of crossbar current when mapping MVM operations to hardware.

As shown in Fig. 5, the stochastic network is trained to generate a broader distribution, covering more non-ternary values, which makes leveraging the stochastic switching possible. The deterministic 1-bit sense amplifier (SA) model trains to generate a narrower

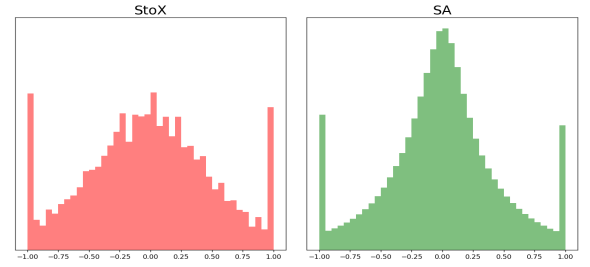


**Figure 5:** The distribution of normalized array-level MVM outputs collected in a DNN model trained with stochastic MTJs ("StoX") compared with a model with sense amplifier (SA) behavior.

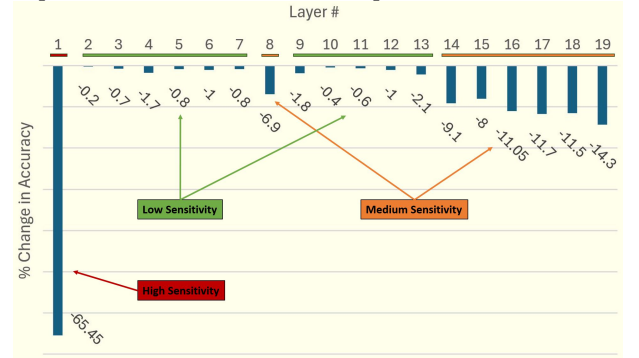


**Figure 6:** Monte Carlo simulation for determination of the most important StoX-Net layers to create a multisampling schedule for optimizing accuracy and latency

Gaussian distribution around 0 and a concentration at -1 and 1. During the MTJ conversion, the accumulated analog current supplied to the heavy metal layer of SOT-MTJ will be converted to bi-stable states, which are interpreted as (-1, 1) for better representation in training [27].

To mitigate the errors due to stochastic bit generation, we leverage multisampling to recover accuracy with some trade-off of hardware efficiency. More SOT-MTJ samples will lead to a better representation of the analog output. We explored no more than 8 samples per conversion since the total conversion energy and latency increase linearly with the number of samples.

Additionally, we perform a Monte Carlo simulation on our network's trainable StoX layers to guide an inhomogeneous multisampling scheme. For each layer, we apply a uniform random perturbation to its weights at inference and then measure the significance of the weights of that layer to the model performance, which is represented by the accuracy loss. Fig. 6 shows the first layer being most susceptible to perturbation, indicating the most significance, while layers close to the output classifications are moderately susceptible to error as well. Based on this analysis, we implement a model with mixed layer-wise sampling numbers ("Mix-QF"), where layers with higher sensitivity utilize more samples and layers with lower sensitivity fewer samples. We achieve an accuracy similar to a homogeneous 4-sample network with only a small increase in operations compared to the 1-sample network. For maintaining higher accuracy and decreasing overhead, only layers that *require* extra samples are given multisampling in our study.

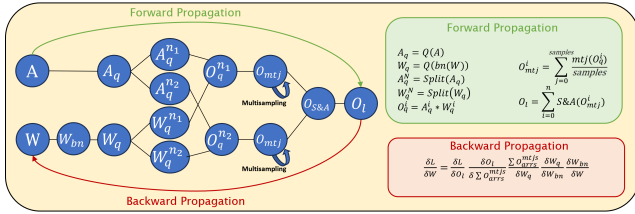


**Figure 7:** A simplified overview of StoX-Net's convolutional forward and backward propagation

During backward propagation, the loss  $\frac{\partial L}{\partial W_l}$  across a single convolutional layer with partial sums follows the high-level representation in Fig. 7 and is shown in-depth via the following equations:

$$\frac{\partial L}{\partial W_l} = \frac{\partial L}{\partial O_l} \sum_{i=1}^{N_{arrs}} \sum_{j=1}^{samples} \frac{\partial O_l^{i,j}}{\partial W_l}. \quad (2)$$

Where  $O_l$  is the layer's final output obtained from the S&A summation of all array-level output  $O_{i,j}$  (each sample  $i$  and each subarray  $j$ ). For each S&A subarray output vector and its respective MTJ samples, the gradient needs to be calculated as:

$$\frac{\partial O_l^{i,j}}{\partial W_l} = \frac{\partial O_l^{i,j}}{\partial O_{S\&A}^{i,j}} \frac{\partial O_{S\&A}^{i,j}}{\partial O_{MTJ}^{i,j}} \frac{\partial O_{MTJ}^{i,j}}{\partial O_q^i} \frac{\partial O_q^i}{\partial W_q^i} \frac{\partial W_q^i}{\partial W_{bn}} \frac{\partial W_{bn}}{\partial W_l}. \quad (3)$$

Equation 3 considers the S&A, MTJ, weight quantization, array-splitting, and normalization algorithms with respect to the layer's weights. We approximate the MTJ's gradient using a straight-through estimator (STE), and clamp values outside its saturation range to avoid exploding gradients. The weight quantization's gradients are similar to that of [16]. Considering all of these, the gradient for backward propagation can be reduced to:

$$\frac{\partial L}{\partial W} = \frac{\partial L}{\partial O_l} \frac{\partial O_l}{\partial \sum O_{arrs}^{mtjs}} \frac{\partial \sum O_{arrs}^{mtjs}}{W_q} \frac{W_q}{W_{bn}} \frac{W_{bn}}{W}, \quad (4)$$

as shown in Fig. 7.

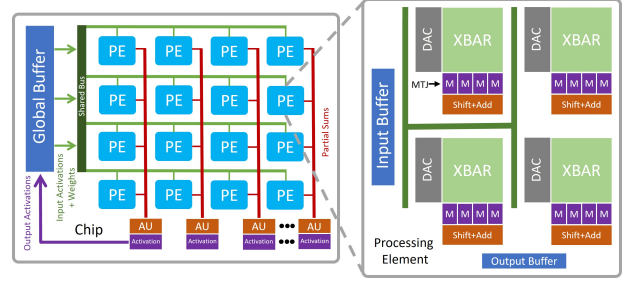


**Figure 8:** Evaluated In-Memory Computing System

## 4 EXPERIMENTAL RESULTS: FUNCTIONAL ACCURACY AND HARDWARE EFFICIENCY

### 4.1 Evaluation Methodology

We evaluate both the functional accuracy and hardware efficiency of the proposed StoX-Net designs, including both a quantized first layer (QF) and a high-precision first layer (HPF), while other subsequent layers adopt the MTJ-based stochastic conversion. All QF models take 8 samples per MTJ conversion in the first layer due to its importance shown by the Monte Carlo analysis in Fig. 6. We compare StoX-Net with a standard IMC featuring a high-precision ADC for all layers (HPFA). We also include an IMC design with sparse ADC (SFA) as a strong baseline for hardware comparison, where we reduce the precision of the ADC by 1 from the full precision ADC in HPFA. We investigate the impact of hardware and software configurations, including array sizes, weight bit precision,  $\tanh$  sensitivity parameter, and the number of MTJ samples across the study.

We denote X-bit weight, Y-bit activation, and Z-bits per slice as  $XwYaZb_s$ . For example, 4-bit weight, 4-bit activation, and 2-bits per slice are  $4w4a2b_s$ . Unless otherwise specified, the baseline StoX network can be assumed, having characteristics of  $4w4a4b_s$ ,  $\alpha = 4$ ,  $R_{arr} = 256$ , 1 sample per MTJ, and HPF. Networks will only be described by their difference from this baseline. For example, 1-QF uses the stochastic MTJ converter with 1 sample in all layers except the first, which would have an MTJ converter with 8 samples. 4-HPF uses a high-precision ADC in the first layer and 4 samples of the stochastic converter in all other layers. Layers with high- $\alpha$  will not see multisampling as such hardware is deterministically binary.

For StoX-Net's accuracy measurements, we train Resnet-20 models based on the proposed convolutional methodology in Section 3. For CIFAR-10, we train with hyperparameters similar to [16], and for MNIST we lower epochs from 400 to 25.

For evaluating hardware efficiency, we simulate a simple IMC architecture similar to that of ISAAC [19], as shown in Fig. 8. To account for both positive and negative input activations and weights, we follow the representation described in [17]. In this representation, the positive and negative components of the activations are streamed separately. Two bits corresponding to the positive and negative components of each weight bit are stored in a group of two memristor cells. As a result, the current accumulated in each crossbar column, which can be either positive or negative, represents the MVM operation. Hence, the energy and area values for the DAC and crossbar (Xbar) cells are doubled during the hardware evaluation. We create our architecture models using Accelergy/Timeloop [15, 24, 25]. We use ReRAM devices with ( $R_{LRS}$ ) of 500kOhm, and

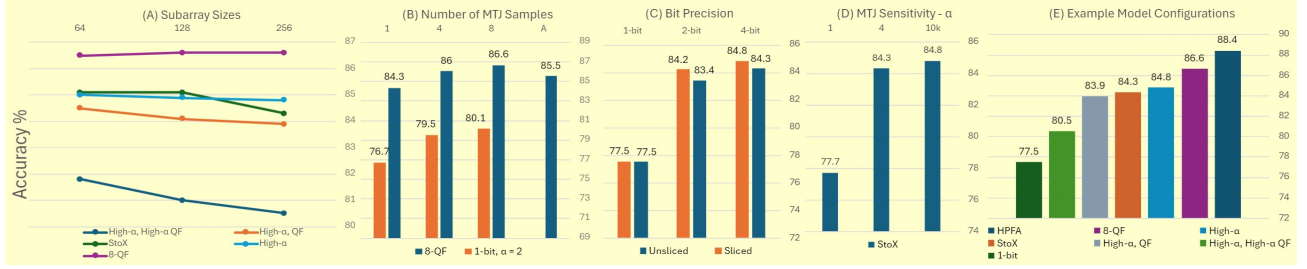


Figure 9: Accuracy across various configurations and an ablation study of StoX-Net

an  $R_{HRS}/R_{LRS}$  ratio of 10 [2] as the Xbar cells. We use Successive Approximation Register (SAR) ADC with the area and power metrics scaled for 28nm technology based on comprehensive surveys and analysis of ADC architectures [14] [5, 22]. Table 2 summarizes key parameters for the hardware components. Our baseline HPFA architecture results were verified to be consistent with previous works [5][2].

Component	Energy/Action (pJ)	Area/instance ( $\mu m^2$ )
DAC [15]	2.99e-2	0.127
Xbar Cell(1b/2b) [2]	(1.37e-3/0.93e-3)	0.0308
ADC(FP/Sparse) [14]	(2.137/1.171)	(6600/2700)
MTJ-Converter	5.69e-3	0.0163

Table 2: Energy and Area of Simulated Hardware Components

## 4.2 Functional Accuracy

Samples:	StoX-Net			Ref.[17]
	1-QF	4-QF	Mix-QF	HPF
1w1a1b <sub>s</sub>	96.8	97.6	97.2	98.9
2w2a2b <sub>s</sub>	97.7	98.3	97.9	-
2w2a1b <sub>s</sub>	98.0	98.4	98.2	99.0
4w4a4b <sub>s</sub>	97.9	98.5	98.1	99.2
4w4a1b <sub>s</sub>	98.2	98.4	98.3	-

Table 3: StoX-Net implementation of a modified ResNet-20 on MNIST Handwritten Digits with  $R_{arr} = 128$ .

Samples	StoX-Net				Ref. [17]	Ref. [16]
	1	4	8	Mix	High- $\alpha$ HPF	
QF	76.1	83.3	<b>83.8</b>	80.6	-	-
HPF	84.3	<b>86.0</b>	<b>86.6</b>	<b>85.5</b>	84.2	85.4

Table 4: StoX 4w4a4b<sub>s</sub> Resnet-20 on CIFAR-10 @  $R_{arr} = 256$ .

As summarized in Tables 3 & 4, the proposed StoX-Net can reach within 1% of the reference HPF model’s accuracy for both MNIST and CIFAR-10 datasets. As shown in Fig. 9A, large arrays suffer small accuracy loss as the stochastic conversion is applied to an increased range of possible crossbar output values, losing information. Bit slicing is shown to moderately mitigate the accuracy degradation of quantization (Fig. 9B). Most notably, *stochastic multisampling consistently mitigates accuracy loss*.

In Fig. 9E, "high- $\alpha$ , high- $\alpha$  QF" implements step-like sense amplifier to quantize *all layers including the first conv layer*. Comparatively, by enabling a stochastic first layer, "high- $\alpha$ , QF" experiences immediate (over 3.4%) accuracy improvement, with 8 samples for the first *StoX conv* (see the bright-green and grey bars). Such observation demonstrates that our stochastic MTJ enables an effective quantization of the first *conv* layer through its increased representational capability.

We also observe that while larger  $\alpha$  (step-like) might be preferred for 1-time sampling (Fig. 9D), higher accuracy can be obtained through multisampling (Table 4), such as 4 or 8 samples, of a smaller  $\alpha$  (stochastic). The configuration of layer-wise mixed samplings ("Mix-QF") only increases the number of MVM conversions by 14.3% compared to the 1-sample model but reaches 85.5% accuracy near the 4-sample network. As discussed in the following section, although sampling multiple times monotonically increases the energy and latency, our 4-QF configuration that uses 4 samples per MTJ conversion still achieves  $\sim 100x$  improvement in EDP.

## 4.3 Hardware Efficiency

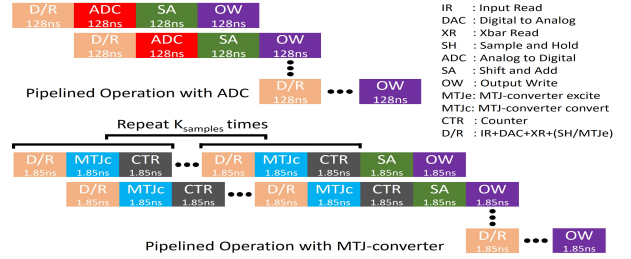
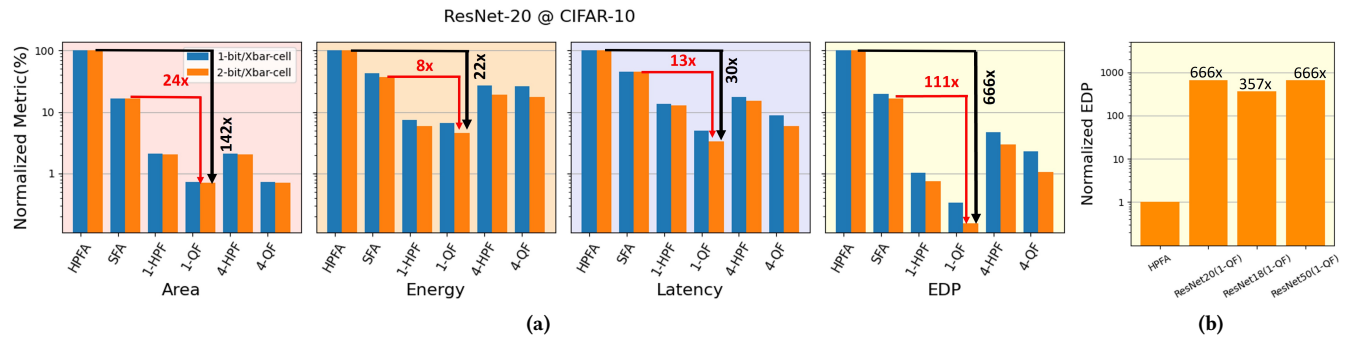


Figure 10: Pipelined MVM operation in a crossbar IMC using ADC versus using MTJ-converter

It is important to note that our area-efficient and highly parallel PS processing directly impacts the datapath design pattern of crossbar MVM operation. Fig. 10 shows the pipelined operations inside a crossbar using an ADC (top) and a stochastic MTJ converter (bottom). In standard IMC, the length of each pipeline stage is determined by the longest stage, i.e. the ADC readout of all shared columns in a crossbar. Our optimization alleviates the throughput bottleneck by parallelizing all columns with compact MTJ converters, thereby considerably reducing the length of the pipeline stage (from 128 ns to 1.85 ns in our case). However, increasing the number of samples reduces such throughput benefits and creates a trade-off between latency and accuracy.

Our hardware performance evaluation is summarized in Fig. 11. Full precision ADC (HPFA) and Sparse design (SFA) are our



**Figure 11:** Hardware efficiency, evaluated by simulating an ISAAC-like IMC architecture in Timeloop [15]. (11a) Normalized metrics between the baseline configurations and optimized configurations running ResNet-20 on CIFAR-10. (11b) EDP improvement of ResNet-20 on CIFAR-10, ResNet-18 and ResNet-50 on Tiny ImageNet compared to respective baseline (HPFA).

baselines for comparison. The first observation is that SOT-MTJ converters significantly enhance parallelism without large area overhead, showing large savings in area and EDP. Our proposed hardware design can offer area, energy, and latency reduction of up to 142x, 22x, and 30x, respectively. Our design achieves up to 111x (666x) EDP improvement compared to an IMC with sparse (full-precision) ADC. We further demonstrate in Fig. 11b that our architecture can be scaled to larger models and workloads while maintaining remarkable efficiency improvement. Moreover, the multisampling feature of our proposed stochastic converter offers the flexibility to trade off EDP gain in exchange for improved accuracy.

## 5 CONCLUSION

We develop StoX-Net, an efficient IMC design that eliminates the ADC bottleneck by processing array-level partial sum using probabilistic switching of MTJ. The proposed IMC co-design framework reaches close to the state-of-the-art accuracy at CIFAR-10 classifications while achieving over 140x area efficiency and 100-600x improvement in hardware efficiency characterized by EDP. Moreover, leveraging the multisampling capability of stochastic MTJ converters, quantizing the first convolution layer, which is costly in prior quantization-aware training, was demonstrated to have less than 2% accuracy loss. Our work suggests exciting opportunities for utilizing stochastic computation and spintronics for developing next-generation AI hardware accelerators.

## REFERENCES

- [1] 2004. *MOSIS Scalable CMOS (SCMOS) Design Rules (Revision 8.0)*. <https://www10.edacafe.com/book/ASIC/CH02/CH02.3.php>
- [2] Aayush Ankit, et al. 2019. PUMA: A programmable ultra-efficient memristor-based accelerator for machine learning inference. In *24th ASPLOS*. 715–731.
- [3] I. Chakraborty, et al. 2020. Resistive crossbars as approximate hardware building blocks for machine learning: Opportunities and challenges. *Proc. IEEE* (2020).
- [4] B. Fleischer and others. IBM Research Blog, 2020. Unlocking the Promise of Approximate Computing for On-Chip AI Acceleration.
- [5] Kang He, et al. 2022. Design Space and Memory Technology Co-Exploration for In-Memory Computing Based Machine Learning Accelerators. In *IEEE/ACM ICCAD (ICCAD '22)*. Article 91, 9 pages. <https://doi.org/10.1145/3508352.3549453>
- [6] Sitao Huang, et al. 2021. Mixed precision quantization for ReRAM-based DNN inference accelerators. In *ASP-DAC*. 372–377.
- [7] Jimmy J. Kan, et al. 2017. A Study on Practically Unlimited Endurance of STT-MRAM. *IEEE Transactions on Electron Devices* 64, 9 (2017), 3639–3646.
- [8] Dong Eun Kim, et al. 2023. SAMBA: Sparsity Aware In-Memory Computing Based Machine Learning Accelerator. *IEEE Trans. Comput.* (2023).
- [9] Hyungjun Kim, et al. 2020. Algorithm/hardware co-design for in-memory neural computing with minimal peripheral circuit overhead. In *2020 57th ACM/IEEE DAC*. IEEE, 1–6.
- [10] Yulhwa Kim, et al. 2018. Neural Network-Hardware Co-design for Scalable RRAM-based BNN Accelerators. *ArXiv abs/1811.02187* (2018).
- [11] Yulhwa Kim, et al. 2022. Extreme partial-sum quantization for analog computing-in-memory neural network accelerators. *ACM JETC* 18, 4 (2022), 1–19.
- [12] Yulhwa Kim, et al. 2021. Mapping Binary ResNets on Computing-In-Memory Hardware with Low-bit ADCs. In *2021 DATE*. 856–861.
- [13] Zechun Liu, et al. 2018. Bi-real net: Enhancing the performance of 1-bit cnns with improved representational capability and advanced training algorithm. In *ECCV*. 722–737.
- [14] Boris Murmann. [n. d.]. ADC Performance Survey 1997-2023. [Online]. Available: <https://github.com/bmurmann/ADC-survey>.
- [15] Angshuman Parashar, et al. 2019. Timeloop: A Systematic Approach to DNN Accelerator Evaluation. In *2019 IEEE ISPASS*. 304–315.
- [16] Haotong Qin, et al. 2020. Forward and Backward Information Retention for Accurate Binary Neural Networks. In *2020 IEEE/CVF CVPR*. 2247–2256.
- [17] Utkarsh Saxena, et al. 2022. Towards ADC-Less Compute-In-Memory Accelerators for Energy Efficient Deep Learning. In *2022 DATE*. 624–627.
- [18] Abhronil Sengupta, et al. 2016. Magnetic tunnel junction mimics stochastic cortical spiking neurons. *Scientific reports* 6, 1 (2016), 30039.
- [19] Ali Shafiee, et al. 2016. ISAAC: A convolutional neural network accelerator with in-situ analog arithmetic in crossbars. *ACM SIGARCH Comp. Arch. News* (2016).
- [20] Tanvi Sharma, et al. 2021. Enabling Robust SOT-MTJ Crossbars for Machine Learning using Sparsity-Aware Device-Circuit Co-design. In *IEEE/ACM ISLPED*.
- [21] Gopalakrishnan Srinivasan, et al. 2017. Magnetic tunnel junction enabled all-spin stochastic spiking neural network. In *Design, Automation & Test in Europe Conference & Exhibition (DATE), 2017*. IEEE, 530–535.
- [22] Qian Wang, et al. 2016. Neuromorphic processors with memristive synapses: Synaptic interface and architectural exploration. *ACM Journal on Emerging Technologies in Computing Systems (JETC)* 12, 4 (2016), 1–22.
- [23] Zhaohao Wang, et al. 2015. *STT SOT MTJ*. [http://www.spinlib.com/STT\\_SOT\\_MTJ.html](http://www.spinlib.com/STT_SOT_MTJ.html)
- [24] Yannan Nellie Wu, et al. 2019. Accelergy: An Architecture-Level Energy Estimation Methodology for Accelerator Designs. In *2019 IEEE/ACM ICCAD*. 1–8.
- [25] Yannan Nellie Wu, et al. 2020. An Architecture-Level Energy and Area Estimator for Processing-In-Memory Accelerator Designs. In *2020 IEEE ISPASS*. 116–118.
- [26] Tzu-Hsien Yang, et al. 2019. Sparse reram engine: Joint exploration of activation and weight sparsity in compressed neural networks. In *ISCA*. 236–249.
- [27] Shien Zhu, et al. 2020. XOR-Net: An Efficient Computation Pipeline for Binary Neural Network Inference on Edge Devices. In *2020 IEEE ICPADS*. 124–131.